Available online at www.sciencedirect.com
ScienceDirect
Journal of Power Sources 178 (2008) 141–150
JOURNAL OF POWER SOURCES
www.elsevier.com/locate/jpowsour

A PEM fuel cell model for cold-start simulations

Hua Meng *

Center for Engineering and Scientific Computation, School of Aeronautics and Astronautics, P.O. Box 1455, Zhejiang University, Hangzhou, Zhejiang 310027, PR China

Received 29 October 2007; received in revised form 10 December 2007; accepted 10 December 2007
Available online 23 December 2007

Abstract

In this paper, a transient multiphase multi-dimensional PEM fuel cell model has been developed in the mixed-domain framework for elucidating the fundamental physics of fuel cell cold start. Cold-start operations of a PEM fuel cell at a subfreezing boundary temperature of −20 °C under both constant current and constant cell voltage conditions have been numerically examined. Numerical results indicate that the water vapor concentration inside the cathode gas channel affects ice formation in the cathode catalyst layer and thus the cold-start process of the fuel cell. This conclusion demonstrates that high gas flow rates in the cathode gas channel could increase fuel cell cold-start time and benefit the cold-start process. It is shown that the membrane plays a significant role during the cold-start process of a PEM fuel cell by absorbing the product water and becoming hydrated. The time evolutions of ice formation, current density and water content distributions during fuel cell cold-start processes have also been discussed in detail.

Keywords: Cold start; Subfreezing temperature; Ice formation; Mixed-domain model; Constant current density; Constant cell voltage

1. Introduction

PEM fuel cells as future automotive power plants have to be able to start up successfully from subfreezing temperatures and simultaneously maintain the cell integrity and performance. In order to meet these critical requirements, substantial research efforts have recently been expended to investigate cold-start phenomena and freezing processes in PEM fuel cells.

Cho et al. [1] studied the PEM fuel cell characteristics after repetitive freeze/thaw thermal cycling between 80 and −10 °C. It was found that the cell performance degraded with the increased polarization resistance and ohmic losses after a number of thermal cycles. They concluded that the increase of the polarization resistance could be attributed to the deformation of the electrode structure, while the increase in the ohmic resistance was mainly due to the increase of the contact resistance between the membrane and the electrode. Both phenomena were caused by the volume dilatation during the freezing process. In order to prevent PEM fuel cell performance degradation after the freeze/thaw cycling, Cho et al. [2] later successfully applied the gas-purging method, by which water was removed from the fuel cell through feeding dry gases to the cell, and the solution-purging method by using an anti-freeze solution instead of the dry gases.

Hou et al. [3] also demonstrated that with appropriate gas purging, no performance degradation and MEA delamination in a PEM fuel cell would occur after 20 freeze/thaw cycles from −20 to 60 °C. The experimental studies of McDonald et al. [4] indicated that with membranes and MEAs assembled under ambient humidity conditions resulting in low water contents, no catastrophic physical or chemical failures were observed in the fuel cell membrane after repetitive freeze/thaw cycles.

In order to examine basic cold-start behaviors of PEM fuel cells, Oszcipok et al. [5] conducted isothermal potentiostatic cold-start measurements of a single cell. It was shown that the product water initially increased the membrane humidity at subfreezing temperatures, and after the membrane humidity reached its maximum, the product water would flood the catalyst layer and the gas diffusion layer (GDL) and become frozen. Ice formation would subsequently lead to strong current density decay and cell degradation. They also carried out a mathematic curve fitting and statistic regression analyses, and showed that dryer membrane and high gas flow rates would benefit the PEM fuel cell cold-start operations. Oszcipok et al. [6] further developed a physical PEM fuel cell model to describe the transient behav-

* Tel.: +86 571 87952990; fax: +86 571 87953167.
E-mail address: menghua@zju.edu.cn.

0378-7753/$ – see front matter © 2007 Elsevier B.V. All rights reserved.
doi:10.1016/j.jpowsour.2007.12.035

Nomenclature

a	water activity or surface area
c	molar concentration (mol m^{-3})
C_p	constant-pressure heat capacity (J kg^{-1} K^{-1})
D	mass diffusivity (m^2 s^{-1})
D_λ	water content diffusivity (mol m^{-1} s^{-1})
EW	equivalent weight of the membrane (kg mol^{-1})
F	Faraday constant (96487 C mol^{-1})
h_{vi}	enthalpy of desublimation (J kg^{-1})
i	current density (A m^{-2})
j	transfer current density (A m^{-3})
k	thermal conductivity (W m^{-1} K^{-1})
k_c	desublimation rate coefficient (s^{-1})
K	permeability (m^2)
n_d	electro-osmotic drag coefficient
p	gas-phase pressure (Pa)
R_u	universal gas constant (J mol^{-1} K^{-1})
s_{ice}	ice fraction
S	source term
t	time (s)
T	temperature (K)
u	gas-phase velocity (m s^{-1})
U_o	open-circuit potential (V)
V	volume (m^3)
V_{cell}	cell voltage (V)
W	molecular weight (kg mol^{-1})

Greek letters

ε	porosity
ε_m	fraction of the membrane phase in the catalyst layer
η	over-potential (V)
κ	proton conductivity (S m^{-1})
λ	water content
μ	viscosity (kg m^{-1} s^{-1})
ρ	gaseous density (kg m^{-3})
σ	electronic conductivity (S m^{-1})
τ	viscous stress tensor
Φ	phase potential (V)
χ	mole fraction

Subscripts

cl	catalyst layer
e	electrolyte or energy
i	species
m	membrane
s	electron or solid phase
sat	saturation value
vi	water vapor to ice phase
w	water

Superscripts

cl	catalyst layer
eff	effective value
sat	saturation value
v	vapor phase

iors of a PEM fuel cell under isothermal subzero operations. The model was able to account for the effects of the reduction of the active catalyst surface and the increase of the contact resistance on the cell performance.

Tajiri et al. [7] developed an experimental procedure for elucidating the isothermal PEM fuel cell cold start by introducing a method of equilibrium gas purge using the partially humidified gas with a specified relative humidity to effectively control the initial water distribution inside the cell. During a cell startup from −30 °C under a constant current density, they found that a PEM fuel cell with a low membrane water content experienced three stages of voltage evolution, namely an initial voltage drop, a voltage recovery period resulting from the membrane hydration by the product water, and a final voltage drop-down owing to ice formation and its blockage of species transport and coverage of the active catalyst surface. Tajiri et al. [8] also examined the effects of various parameters on the PEM fuel cell cold-start capability under isothermal conditions, including the purge methods, startup temperature and current density, and the membrane thickness.

Thompson et al. [9] developed an experimental procedure to determine the oxygen reduction reaction (ORR) kinetics in PEM fuel cells at subfreezing temperatures. No fundamental change in the ORR reaction mechanism was found at subfreezing temperatures. Thompson et al. [10] also measured low-temperature proton conductivity in the Nafion membrane as a function of water content and temperature, with temperature ranging from −45 to 25 °C. A crossover in the activation energy for proton transport with temperature coinciding with the melting and freezing of water was found, and the crossover temperature depended on the initial water content of the membrane and displayed a hysteresis phenomenon between heating and cooling processes. However, this observation contradicted that of Tajiri et al. [7], obtained with a temperature range of −30 to 30 °C. Tajiri et al. [7] found no noticeable phase transition of water occurring inside the membrane and thus no slope change in the proton conductivity. Therefore, an uncertainty remains in this area.

Yan et al. [11] investigated PEM fuel cell cold-start behaviors and the effect of the subzero temperature on cell performance using a 25 cm^2 cell. They found that the cell was capable of cold-start operation at −5 °C without irreversible performance loss, but if the cell temperature fell below −5 °C, irreversible performance loss occurred. Significant damages to the membrane electrode assembly (MEA) and backing layer were observed after the fuel cell operated at temperatures below −5 °C, including the catalyst layer delamination from the membrane and cracks in the membrane.

Ge and Wang [12] conducted visualization experiments on liquid water transport and ice formation using a transparent PEM fuel cell. It was concluded that the freezing-point depression of water in the cathode catalyst layer should be less than 2 °C and its role in cold-start practice should thus be negligible. They later further narrowed down the value range to 1.0 ± 0.5 °C [13]. It should be noted that this conclusion contradicts that of Ishikawa et al. [14], who found that water existed in the super-cooled liquid state when a PEM fuel cell was operated at −10 °C.

Therefore, more research work is needed in this area for further clarification. However, all the studies have observed that no matter which phase of water, liquid water droplets or ice particles, existed, it could appear on the catalyst surface only after a period of cell operation after the membrane became hydrated.

In parallel to experimental studies, numerical investigations have also been conducted. A number of research groups focused on modeling the stack behaviors during cold-start operations. Sundaresan and Moore [15] developed a stack thermal model to study PEM fuel cell cold start. They focused on a layered model, which separated the stack into different layers, to determine the temperature distribution within the stack. The model could reveal the effects of the endplate thermal mass and the internal heating method on the stack cold-start operations. Khandelwal et al. [16] developed a one-dimensional thermal model for a PEM fuel cell stack to investigate the cell cold-start capability and the corresponding energy requirement at various operating and ambient conditions. They observed that an optimum range of operating current density existed for a given stack design for rapid cold startup and recommended thermal isolation of the stack at the endplates to reduce the startup time. It was also found that flow of heated coolant above 0 °C was an effective way to achieve rapid stack cold start.

Ahluwalia and Wang [17] developed a simple two-dimensional model of a single cell for simulating PEM fuel cell cold start. It was shown that for rapid and robust cell self-start, operation of the fuel cell near the short-circuit condition was desirable because of its maximum hydrogen utilization and favorable waste heat production. They concluded that preheating the feed gases, electrically heating the cell stack, and the cell operating pressure produced only small effects on the ability of the cell self-start and startup time.

Mao and Wang [18] developed a lumped analytical model to study heat balance, ice formation in the cathode catalyst layer, water transport, and voltage variation during a PEM fuel cell cold start from −10 and −20 °C. The key parameters controlling PEM fuel cell cold-start operations, including the initial membrane water content and the thermal mass of the bipolar plates, were investigated. Mao and Wang [19] further developed a detailed transient multiphase multi-dimensional PEM fuel cell model within the single-domain framework for cold-start simulations. The model incorporated various transport phenomena and accommodated ice formation by assuming instantaneous desublimation of water vapor after it reaches its saturation value, which should be physically valid based on the visualization work of Ge and Wang [12,13]. The three-dimensional results, calculated under a constant current density, illustrated distributions of current density, temperature, membrane water content, and ice fraction in the cathode catalyst layer. The effects of the startup current density and membrane thickness on cell cold-start behaviors were also examined.

In this paper, a transient multiphase multi-dimensional PEM fuel cell model, based on the previously established mixed-domain approach [20–23], has been developed for elucidating fuel cell cold-start behaviors. Cold-start operations of a PEM fuel cell at a subfreezing boundary temperature of −20 °C under both constant current and constant cell voltage conditions have been numerically investigated, focusing on a two-dimensional configuration for fundamental physical understandings and clear result presentation.

2. Theoretical formulation

The transient multiphase multi-dimensional PEM fuel cell model accommodating ice formation is developed based on a previously established transient two-phase multi-dimensional mixed-domain approach [23] and is briefly described in this section. This numerical model is intended for simulating the isothermal cold start of a PEM fuel cell at a subzero boundary temperature, i.e. −20 °C, under both constant current and constant cell voltage conditions. As in the modeling work of Mao and Wang [19], an assumption of instantaneous desublimation of water vapor to ice has been taken in the present formulation. Based on the visualization data of Ge and Wang [12,13], this assumption could be physically justified below a cell temperature of −3 °C. Therefore, in the present PEM fuel cell model for cold-start simulations, no liquid water exists at the subfreezing cell temperature.

First, the transient conservation equations in the gaseous phase are presented.

Mass conservation:

$$\frac{\partial[\varepsilon(1-s_{\text{ice}})\rho]}{\partial t} + \nabla(\rho\vec{u}) = 0 \tag{1}$$

Momentum conservation:

$$\frac{1}{\varepsilon(1-s_{\text{ice}})}\frac{\partial(\rho\vec{u})}{\partial t} + \frac{1}{\varepsilon^2(1-s_{\text{ice}})^2}\nabla(\rho\vec{u}\vec{u}) = -\nabla p + \nabla\tau + S_u \tag{2}$$

Species conservation:

$$\frac{\partial[\varepsilon^{\text{eff}}(1-s_{\text{ice}})c_i]}{\partial t} + \nabla(\vec{u}c_i) = \nabla(D_i^{\text{eff}}\nabla c_i) + S_i \tag{3}$$

In Eq. (3), according to the mixed-domain approach [20,21], the water vapor concentration is solved only in the gas channels, gas diffusion layers, and catalyst layers on both the anode and cathode sides. In the two catalyst layers, the dissolved water phase (water in the membrane phase) is assumed to be in thermodynamic phase equilibrium with water vapor, and its transport process is combined into the water vapor transport equation using the following water diffusivity [20,21]:

$$D_{\text{w}}^{\text{cl}} = \varepsilon_{\text{cl}}^{1.5}(1-s_{\text{ice}})^{1.5}D_{\text{w}}^{\text{cl},g} + \varepsilon_{\text{m}}^{1.5}D_\lambda\frac{R_{\text{u}}T}{p_{\text{sat}}}\frac{\text{d}\lambda}{\text{d}a} \tag{4}$$

The effective porosity in Eq. (3) for water transport, ε^{eff}, could be modified as

$$\varepsilon^{\text{eff}} = \varepsilon + \frac{\varepsilon_{\text{m}}}{(1-s_{\text{ice}})}\frac{\rho_{\text{m}}}{\text{EW}}\frac{R_{\text{u}}T}{p_{\text{sat}}}\frac{\text{d}\lambda}{\text{d}a} \tag{5}$$

For the other species transport equations, the effective porosity remains as

$$\varepsilon^{\text{eff}} = \varepsilon \tag{6}$$

Table 1
Electrochemical and physical relationships

Description	Expression	Unit
Transfer current density	$j = a^{\text{eff}} j_{0,a}^{\text{ref}} \left(\frac{c_{\text{H}_2}}{c_{\text{H}_2,\text{ref}}}\right)^{1/2} \left(\frac{\alpha_a+\alpha_c}{RT} F\eta\right)$ in anode side $j = a^{\text{eff}} j_{0,c}^{\text{ref}} \left(\frac{c_{\text{O}_2}}{c_{\text{O}_2,\text{ref}}}\right) \exp\left(-\frac{\alpha_c}{RT} F\eta\right)$ in cathode side	A m^{-3}
Over-potential	$\eta = \phi_s - \phi_e$ in anode side $\eta = \phi_s - \phi_e - U_o$ in cathode side	V
Open-circuit potential	$U_o = 1.23 - 0.9 \times 10^{-3}(\text{T}-298)$	V
Electro-osmotic drag coefficient	$n_d = \begin{cases} 1.0 \text{ for } \lambda \le 14 \\ 1.5/8(\lambda - 14) + 1.0 \text{ otherwise} \end{cases}$	
Water activity	$a = \frac{C_w R_u T}{p^{\text{sat}}}$	
Water saturation pressure	$\log_{10} p^{\text{sat}} = -2.1794 + 0.02953(T - 273.15) - 9.1837 \cdot 10^{-5}(T - 273.15)^2 + 1.4454 \cdot 10^{-7}(T - 273.15)^3$	atm
Partial pressure of water vapor	$p^{\text{v}} = C_w R_u T$	Pa
Membrane water diffusivity	$D_w^m = \begin{cases} 3.1 \cdot 10^{-7}\lambda(e^{0.28\lambda} - 1)e^{[-2346/T]} & 0 < \lambda \le 3 \\ 4.17 \cdot 10^{-8}\lambda(1 + 161e^{-\lambda})e^{[-2346/T]} & \text{otherwise} \end{cases}$	$\text{m}^2\,\text{s}^{-1}$
Water content diffusivity	$D_\lambda = \frac{\rho_m}{\text{EW}} D_w^m$	$\text{mol m}^{-1}\,\text{s}^{-1}$
Proton conductivity	$\kappa = (0.5139\lambda - 0.326)\exp\left[1268\left(\frac{1}{303} - \frac{1}{T}\right)\right]$	S m^{-1}

Considering the effect of ice formation, the effective gaseous species diffusion coefficients should be further modified as

$$D_i^{\text{eff}} = D_i \varepsilon^{1.5}(1 - s_{\text{ice}})^{1.5} \tag{7}$$

In addition, ice coverage of the active catalyst surface is modeled using the following linear relationship:

$$a^{\text{eff}} = (1 - s_{\text{ice}})a \tag{8}$$

The effective surface area, a^{eff}, is related to the electrochemical kinetics, as shown in Table 1.

Next, the transient conservation equation of the ice phase can be derived as

$$\frac{\partial(\varepsilon\rho_{\text{ice}} s_{\text{ice}})}{\partial t} = S_{\text{vi}} W_w \tag{9}$$

where the parameter, s_{ice}, is the ice fraction, defined as the ratio of the volume of ice to the pore volume in the porous materials

$$s_{\text{ice}} = \frac{V_{\text{ice}}}{V_p} \tag{10}$$

The volumetric desublimation rate in Eq. (9), S_{vi}, is expressed in the following form:

$$S_{\text{vi}} = h_{pc}(p^{\text{v}} - p^{\text{sat}}) \tag{11}$$

where the desublimation parameter is defined as

$$h_{pc} = \frac{k_c \varepsilon(1 - s_{\text{ice}})x_v}{2R_u T}\left[1 + \frac{|p^{\text{v}} - p^{\text{sat}}|}{p^{\text{v}} - p^{\text{sat}}}\right] \tag{12}$$

This formulation indicates that water vapor would start to freeze after it reaches its saturation value [19]. Combined with the thermodynamic equilibrium assumption, Eq. (5), this formulation would result in the delayed ice precipitation after the membrane phase become hydrated, consistent with the experimental observations [12–14].

The transient water content conservation equation inside the membrane is in the following form:

$$\frac{\partial}{\partial t}\left(\frac{\rho_m \lambda}{\text{EW}}\right) = \nabla(D_\lambda \nabla\lambda) + S_\lambda \tag{13}$$

Since we focus on ice formation in the cathode catalyst layer, the effect of phase transition inside the membrane is neglected in the present numerical investigations. Based on more comprehensive experimental studies, this physical phenomenon could be further considered in the future work.

The transient conservation equation of energy is derived as

$$\frac{\partial}{\partial t}[(\rho C_p)^{\text{eff}} T] + \nabla(\rho C_p \vec{u} T) = \nabla(k^{\text{eff}} \nabla T) + S_T \tag{14}$$

where the effective parameter, $(\rho C_p)^{\text{eff}}$, can be determined in the following general form:

$$(\rho C_p)^{\text{eff}} = \varepsilon(1 - s_{\text{ice}})\rho C_p + \varepsilon s_{\text{ice}}(\rho C_p)_{\text{ice}} + (1 - \varepsilon - \varepsilon_m)(\rho C_p)_s + \varepsilon_m(\rho C_p)_m \tag{15}$$

The source term in Eq. (14) is given as [24]

$$S_T = j\left(\eta + T\frac{\text{d}U_0}{\text{d}T}\right) + \frac{i^2}{\text{cond}} + h_{\text{vi}} W_w S_{\text{vi}} \tag{16}$$

where the second term inside the bracket is considered only on the cathode side. The parameter, cond, in Eq. (16) is either k^{eff} or σ^{eff}, depending on the location in the fuel cell. The last term in Eq. (16) is the heat of desublimation. The related parameters are provided in Table 2. The effective thermal conductivity of each cell layer is approximated as a constant in the present numerical studies and is also listed in Table 2. It should be noted that, in this paper, specific heat capacity, C_p, of the membrane material has been substituted with that of PTFE, since it is not available in the open literature, as also discussed in [25].

Table 2
Physicochemical parameters

Anode volumetric exchange current density, aj_0 (A m^{-3})	1.0E+9
Cathode volumetric exchange current density, aj_0 (A m^{-3})	1.0E+4
Reference hydrogen concentration, c_{H_2} (mol m^{-3})	40
Reference oxygen concentration, c_{O_2} (mol m^{-3})	40
Anode transfer coefficients	$\alpha_a = \alpha_c = 1$
Cathode transfer coefficient	$\alpha_c = 1$
Faraday constant, F (C mol^{-1})	96,487
GDL porosity	0.6
Porosity of catalyst layer	0.2
Volume fraction of ionomer in catalyst layer	0.4
GDL permeability (m^2)	1.0E−12
Catalyst layer permeability (m^2)	1.0E−13
Equivalent weight of ionomer (kg mol^{-1})	1.1
Dry membrane density (kg m^{-3})	1980
Effective electronic conductivity in CL/GDL (S m^{-1})	5000
Operation pressure (atm)	2
Desublimation rate coefficient (s^{-1})	3.0E+7
Thermal conductivity of GDL (Wm^{-1} K^{-1})	1.5
Thermal conductivity of CL (Wm^{-1} K^{-1})	1.5
Thermal conductivity of the membrane (Wm^{-1} K^{-1})	0.5
Enthalpy of desublimation (J kg^{-1})	2.64E+6
Density of carbon material (kg m^{-3})	2200
Density of ice (kg m^{-3})	900
Heat capacity of carbon material (J kg^{-1} K^{-1})	1050
Heat capacity of membrane material (J kg^{-1} K^{-1})	1050
Heat capacity of ice (J kg^{-1} K^{-1})	2100

Finally, the conservation equations of proton and electron transport are derived as [26,27]

Proton transport:

$$\nabla(\kappa^{\text{eff}}\nabla\phi_e) + S_e = 0 \quad (17)$$

Electron transport:

$$\nabla(\sigma^{\text{eff}}\nabla\phi_s) + S_s = 0 \quad (18)$$

Since the electrochemical double layer charging/discharging process is very fast, the transient terms in the two equations can be safely neglected and the two equations thus remain in the steady-state form.

The relevant expressions for the source terms and the other physicochemical relationships can be found in Table 1 and Ref. [22]. The temperature effect on transport parameters has been considered in the present numerical model, but it should be noted that because of the lack of sufficient experimental data and also existing uncertainties in the experimental studies, some of the expressions could be further improved specifically for cold-start simulations, but they should be sufficient for the present parametric studies.

The present numerical model has been applied for simulating PEM fuel cell cold-start operations at a subfreezing boundary temperature under both constant current and constant cell voltage conditions, focusing on a two-dimensional cross section perpendicular to the flow direction, as shown in Fig. 1. The boundary conditions have been defined in Ref. [22] except for the one related to the ice fraction, which can be defined as zero flux at all the five boundaries

$$\nabla s_{\text{ice}} = 0 \quad (19)$$

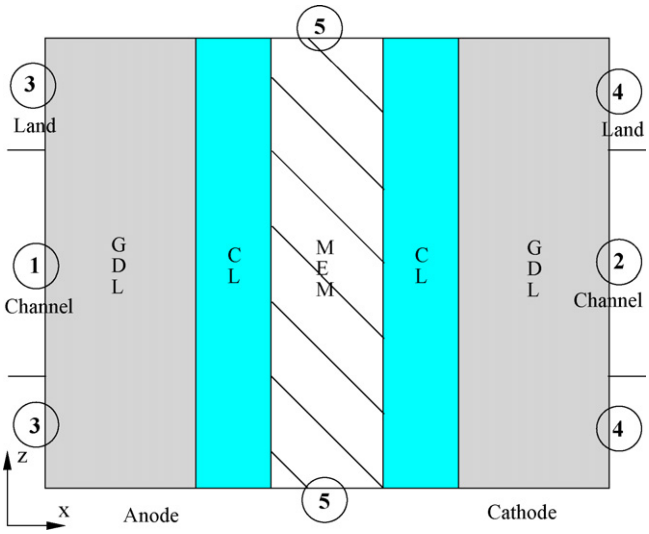

Fig. 1. A two-dimensional cell geometry.

3. Result and discussion

The present PEM fuel cell model for cold-start simulations has been implemented into a commercial CFD package, Fluent, through its user coding capabilities and applied for two-dimensional calculations for elucidating fundamental physics and conducting parametric studies. The geometric configuration is illustrated in Fig. 1, and the geometric parameters are listed in Table 3.

The PEM fuel cell is operated at 2 atm on both the anode and cathode sides. The cell stoichiometry number is two on both sides with a reference current density at 50 mA cm^{-2}. For all the calculations carried out in this paper, the boundary temperature is fixed at −20 °C, simulating an isothermal cold-start condition. Dry hydrogen and dry air are fed into the anode and cathode side, respectively. Based on these operation conditions, the inlet species concentrations can be easily determined and specified at boundaries 1 and 2.

The numerical simulations have been conducted for both a constant current density at 50 mA cm^{-2} and a constant cell voltage at 0.55 V. The fuel cell is purged to an equilibrium condition using a dry gas with 25% relative humidity on both the anode and cathode sides prior to its cold start. Therefore, the initial water content in the membrane can be easily determined and is assumed to be uniformly distributed. The initial ice fraction inside the cell is neglected in the present numerical studies.

Table 3
Cell geometric parameters

Fuel cell geometry (mm)	
Layer thickness	
Diffusion	0.3
Catalyst	0.01
Membrane	0.025
Land width	0.5
Channel width	1.0
Computational cell numbers	∼1600

Careful grid independence study has been conducted [22], and a total of 1600 computational cells are sufficient for obtaining grid-independent solutions in the present numerical simulations. A non-uniform grid system has been employed in the through-membrane direction, with 10 computational cells in the membrane, 10 in each of the gas diffusion layers, and 5 in each of the catalyst layers. Variable time step has been applied with an initial minimum time step at 0.25 s, while it increases gradually to 1 s as the calculation progresses.

Since the water vapor concentration at boundary 2 (an interface between the GDL and gas channel) on the cathode side influences the water vapor distribution inside the cathode catalyst layer and GDL, it significantly affects ice formation and cold-start process of the fuel cell. The effect of the water vapor concentration in the cathode gas channel on ice formation and cell performance is investigated first by defining different water vapor concentrations at boundary 2, which basically represents different downstream locations along the flow direction as the water vapor concentration increases in this direction. This modeling flexibility clearly shows an advantage for elucidating fundamental physics using a two-dimensional configuration.

Under a constant current density at 50 mA cm^{-2}, numerical calculations are conducted with two different water vapor concentrations of 0.074 and 0.033 mol m^{-3} at boundary 2, representing 100% relative humidity and 45% relative humidity in the cathode gas channel at −20 °C, respectively. Transient variations of the cell voltage are depicted in Fig. 2. With a higher water vapor concentration (0.074 mol m^{-3}) defined at boundary 2, the fuel cell cold-start operation shuts down sooner at around 200 s, since in this case the water vapor concentration inside the cathode catalyst layer and GDL reaches its saturation

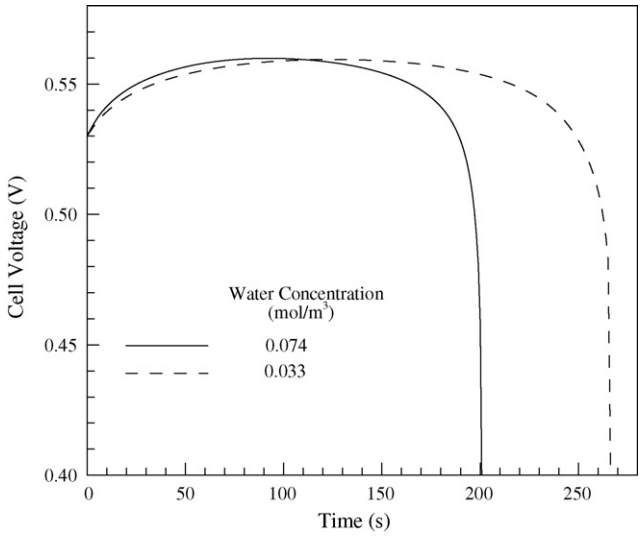

Fig. 2. Time evolution of cell voltage during an isothermal cold start under a constant current density of 50 mA cm^{-2} and different water vapor concentrations at boundary 2.

value and start to freeze earlier. This result indicates that high gas flow rates on the cathode side could increase the fuel cell subzero operation time and benefit the cold-start process, a conclusion consistent with the experimental result of Oszcipok et al. [5].

Transient variations of the cell voltage in Fig. 2 clearly show two-stage evolutions for both cases, namely an initial voltage recovery period owing to the membrane hydration by the product water, and a voltage drop-down period caused by ice formation and its subsequent blockage of oxygen transport and coverage of the active catalyst surface. This trend is consistent with the

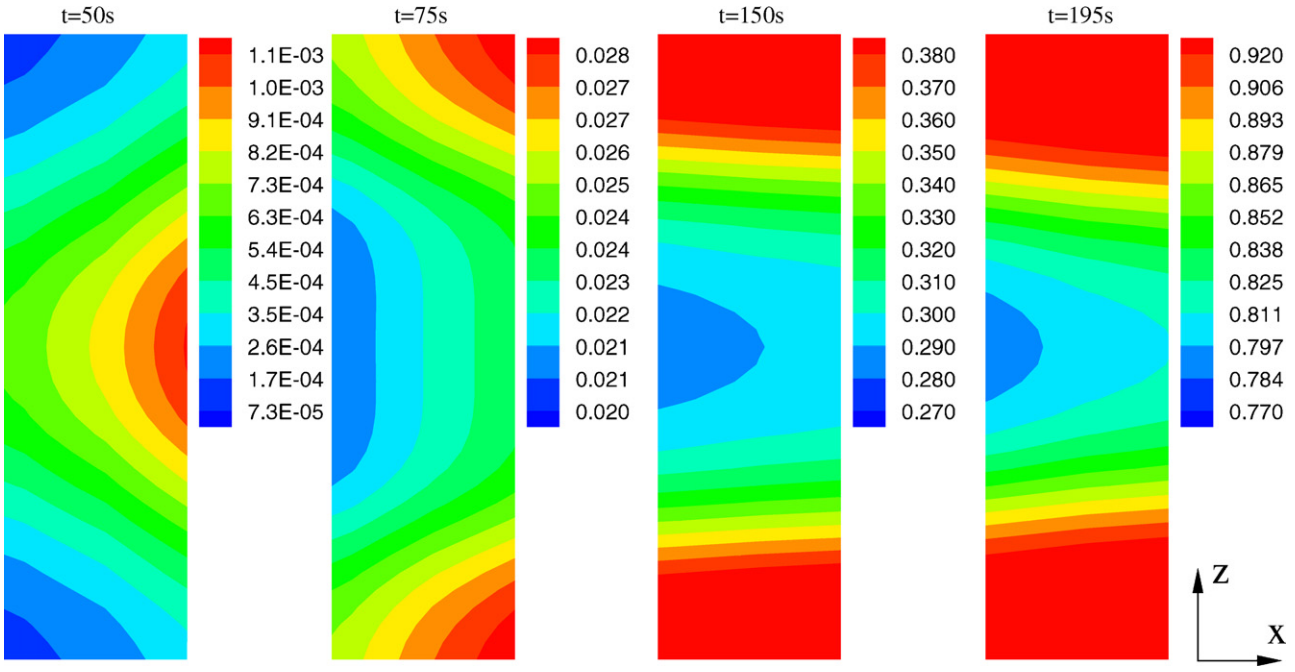

Fig. 3. Time evolution of ice fraction in the cathode catalyst layer during an isothermal cold start under a constant current density of 50 mA cm^{-2} and a water vapor concentration of 0.074 mol m^{-3} at boundary 2.

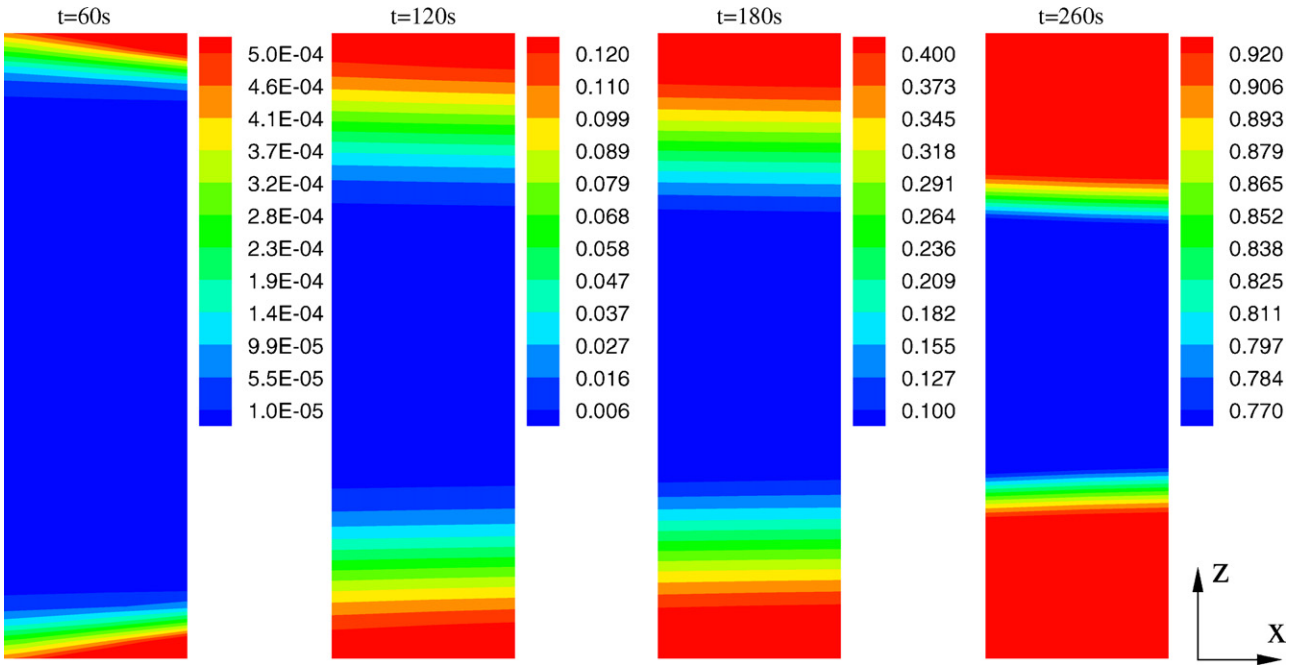

Fig. 4. Time evolution of ice fraction in the cathode catalyst layer during an isothermal cold start under a constant current density of 50 mA cm^{-2} and a water vapor concentration of 0.033 mol m^{-3} at boundary 2.

experimental observation of Tajiri et al. [7]. It should be noted that in the results of Tajiri et al. [7], a three-stage evolution of the cell voltage was observed, but the first stage of the cell voltage drop-down is entirely caused by a gradual load increase, a procedure specifically designed for their experiments but not presently simulated.

As also shown in Fig. 2, during the voltage drop-down period, the cell voltage initially decreases gradually; once the ice fraction in the cathode catalyst layer reaches around 80%, the cell voltage drops dramatically. This phenomenon has also been reported in the work of Mao and Wang [19] and is in a qualitative agreement with the experimental results of Tajiri et al. [7].

The time evolution of the ice fraction in the cathode catalyst layer with a water vapor concentration of 0.074 mol m^{-3} at boundary 2 is illustrated in Fig. 3. Ice starts to precipitate at around 50 s, and grows faster under the current-collecting land. In addition, the numerical results indicate that ice also grows faster at the interface between the catalyst layer and GDL. The reason is that at low current density operations, the electrochemical reaction (ORR) and consequently the water production mainly occur near this location, leading to faster ice formation.

The time evolution of the ice fraction in the cathode catalyst layer with a lower water vapor concentration of 0.033 mol m^{-3} at boundary 2 is further depicted in Fig. 4. By comparing the results in Figs. 3 and 4, the effect of a lower water vapor concentration in the cathode gas channel on ice formation and its evolution can be clearly seen to render lower and more uniform ice fraction directly under the gas channel on the cathode side.

The time evolution of the current density distribution in the lateral direction (z direction) inside the membrane is presented in Fig. 5. Initially (i.e. at 1 s) there is a uniform current density distribution along the lateral direction as defined at boundary 4. With the membrane becomes hydrated by the product water (at 100 s), the current density under the current-collecting land slightly increases, since the membrane water content is higher in this region as shown in Fig. 6. With time further increases, the ice fraction grows faster under the land, as illustrated in Fig. 3, resulting in a rapid drop-down of the current density in this region towards the end of the cold-start process.

The time evolution of the lateral water content distribution in the middle of the membrane is shown in Fig. 6. The water content inside the membrane increases towards the end of the cold-start process, indicating a fraction of the product water is

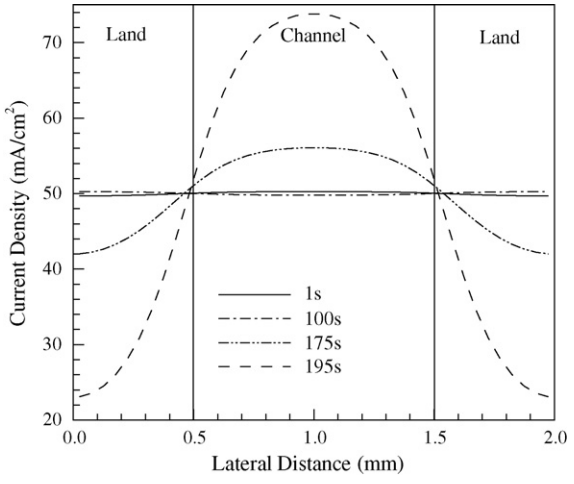

Fig. 5. Transient variation of current density distribution under the same conditions as in Fig. 3.

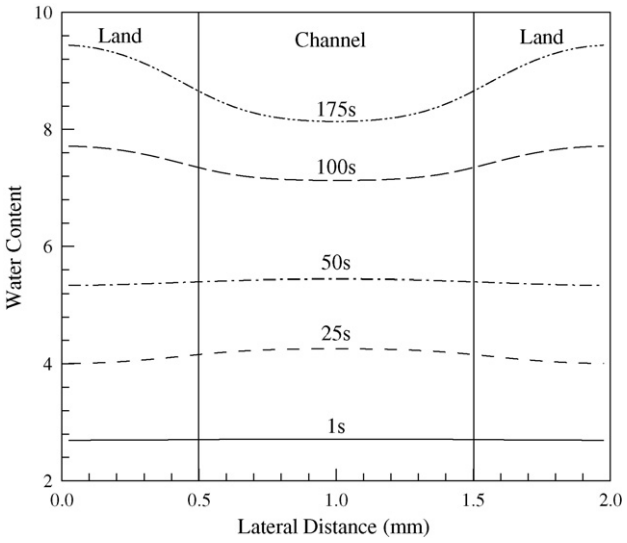

Fig. 6. Transient variation of water content distribution in the middle of the membrane under the same conditions as in Fig. 3.

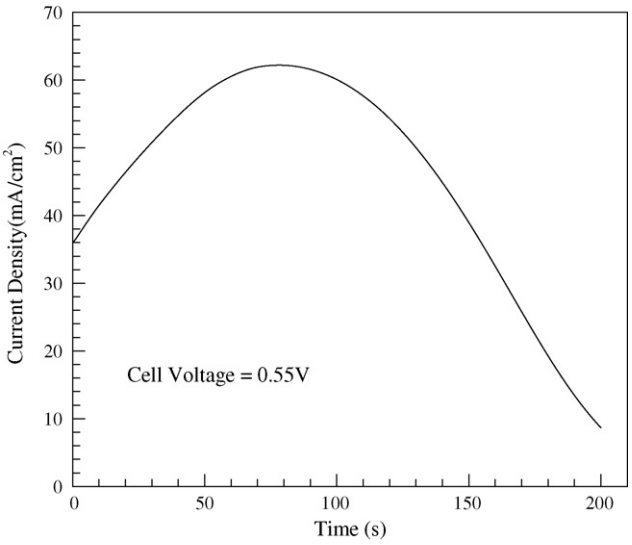

Fig. 8. Time evolution of current density during an isothermal cold start under a constant cell voltage of 0.55 V and a water vapor concentration of 0.074 mol m^{-3} at boundary 2.

absorbed into the membrane and thus the membrane plays a significant role in the cell cold-start process. In addition, Fig. 6 indicates that the water content initially attains a higher value directly under the gas channel inside the membrane, but the trend reverses towards the end of the cold-start process, when more product water is absorbed into the membrane under the current-collecting land.

Fig. 7 illustrates a typical temperature distribution in the two-dimensional cross section. Temperature reaches a highest value in the middle of the cell directly under the gas channel, as expected. The temperature difference across the entire cross plane is, however, very small with the maximum difference at around 0.2 °C. Therefore, the entire cell can be considered to operate under an isothermal condition.

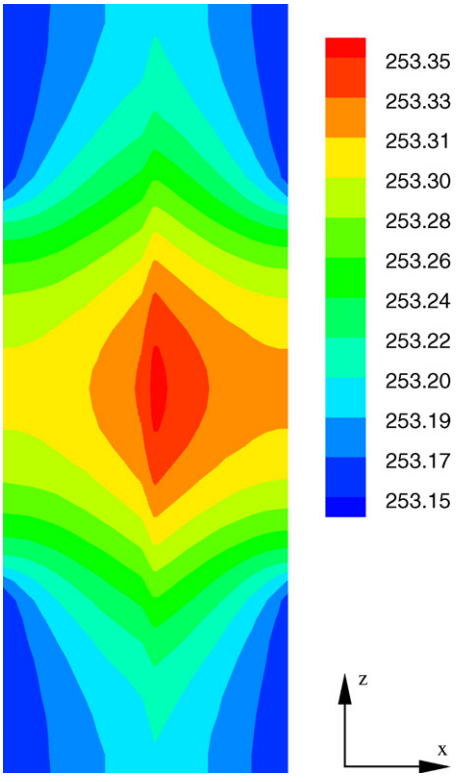

Fig. 7. Temperature distribution in the 2D cross section under the same conditions as in Fig. 3.

The transient variation of the current density during a cold-start operation is shown in Fig. 8, calculated under a constant cell voltage of 0.55 V and with a water vapor concentration of 0.074 mol m^{-3} defined at boundary 2. The result also shows a two-stage evolution; the current density initially increases from 0 s to around 75 s owing to the membrane hydration by the product water, and then gradually decreases due to ice formation. This is in the same general trend as the isothermal potentiostatic cold-start measurements of Oszcipok et al. [5]. However, a rapid drop-down of the current density was observed in the experimental results and was attributed to the increase of the contact resistance between the membrane and the electrode by a statistic regression analysis. Since the transient variation of the contact resistance has not been included in the present numerical model, the rapid current density drop-down cannot be observed in the simulated curve. This difference between the numerical and experimental results, however, indeed confirms the conclusion of Oszcipok et al. [5] that the rapid current density drop-down results from the cell structure changes and the subsequent increase of the contact resistance during the fuel cell cold-start process.

The transient variation of the ice fraction in the cathode catalyst layer calculated under the constant cell voltage condition is illustrated in Fig. 9. In this case, ice starts to precipitate from 50 s after the cold-start process. Ice grows faster under the current-collecting land and accumulates more at the interface between the catalyst layer and GDL, a picture similar to that obtained under the constant current density condition.

The time evolution of the current density distribution inside the membrane is clearly depicted in Fig. 10, under the same

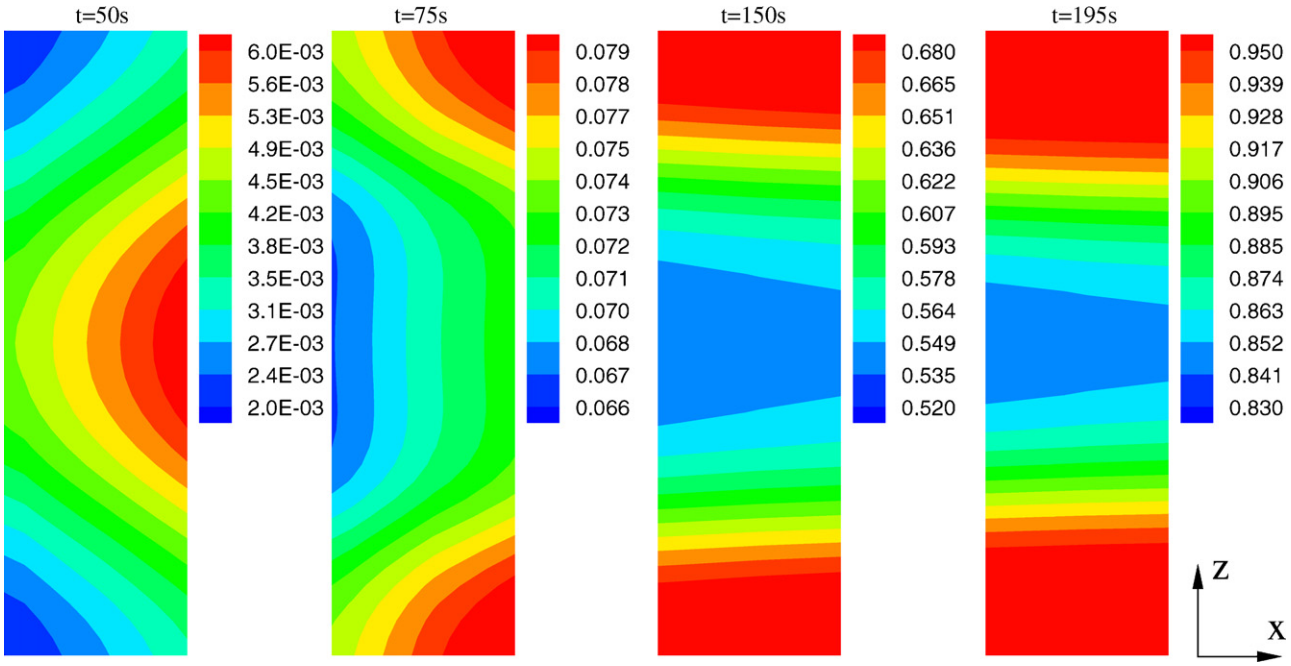

Fig. 9. Time evolution of ice fraction in the cathode catalyst layer under the same conditions as in Fig. 8.

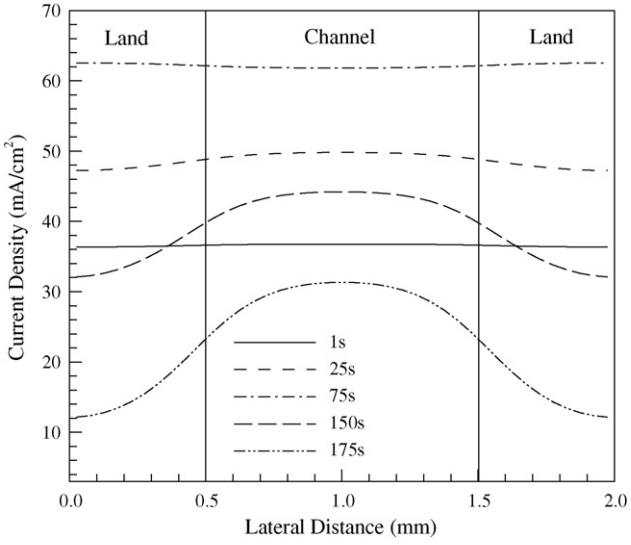

Fig. 10. Transient variation of current density distribution under the same conditions as in Fig. 8.

operation conditions as in Fig. 8. The current density initially distributes uniformly along the lateral direction with an average value at around 36 mA cm^{-2}, it then increases to an average value more than 62 mA cm^{-2} at 75 s. After that, the current density decreases gradually due to ice formation, especially in the regions directly under the current-collecting land.

4. Conclusion

In this paper, a transient multiphase multi-dimensional PEM fuel cell model accommodating ice formation has been successfully developed based on a previously established mixed-domain approach. This model is applied for elucidating fuel cell cold-start processes at a subfreezing boundary temperature of −20 °C. Cold-start operations of a PEM fuel cell under both constant current and constant cell voltage conditions have been numerically investigated.

Numerical results clearly indicate that the water vapor concentration inside the cathode gas channel affects ice formation in the cathode catalyst layer and thus the cold-start process of the fuel cell. This conclusion demonstrates that high gas flow rates in the cathode gas channel could increase fuel cell cold-start time and significantly benefit the cold-start process.

During the cold-start processes under both constant current density and constant cell voltage conditions, the membrane would absorb the product water and become hydrated. Therefore, the membrane plays a significant role during the cold-start process of a PEM fuel cell.

Under both constant current density and constant cell voltage conditions, the cold-start process of a PEM fuel cell with an initial low water content inside the membrane experiences a two-stage evolution; an initial cell performance increase owing to membrane hydration by the product water, and the subsequent performance drop due to ice formation in the cathode catalyst layer and its blockage of oxygen transport and coverage of the active catalyst surface.

In addition, numerical results indicate that ice grows faster in the cathode catalyst layer directly under the current-collecting land and accumulates more at the interface between the cathode catalyst layer and the gas diffusion layer.

Acknowledgement

This work is partially supported by The Ministry of Personnel of PR China and The Department of Personnel of Zhejiang Province (J20070016).

References

[1] E. Cho, J.J. Ko, H.Y. Ha, et al., J. Electrochem. Soc. 150 (2003) A1667.
[2] E. Cho, J.J. Ko, H.Y. Ha, et al., J. Electrochem. Soc. 151 (2004) A661.
[3] J. Hou, H. Yu, S. Zhang, et al., J. Power Sources 162 (2006) 513.
[4] R.C. McDonald, C.K. Mittelsteadt, E.L. Thompson, Fuel Cells 4 (2004) 208.
[5] M. Oszcipok, D. Riemann, U. Kronenwett, et al., J. Power Sources 145 (2005) 407.
[6] M. Oszcipok, A. Hakenjos, D. Riemann, et al., Fuel Cells 7 (2007) 135.
[7] K. Tajiri, Y. Tabuchi, C.Y. Wang, J. Electrochem. Soc. 154 (2007) B147.
[8] K. Tajiri, Y. Tabuchi, F. Kagami, et al., J. Power Sources 165 (2007) 279.
[9] E.L. Thompson, J. Jorne, H.A. Gasteiger, J. Electrochem. Soc. 154 (2007) B783.
[10] E.L. Thompson, T.W. Capehart, T.J. Fuller, et al., J. Electrochem. Soc. 153 (2006) A2351.
[11] Q. Yan, H. Toghiani, Y.W. Lee, et al., J. Power Sources 160 (2006) 1242.
[12] S. Ge, C.Y. Wang, Electrochem. Solid-State Lett. 9 (2006) A499.
[13] S. Ge, C.Y. Wang, Electrochim. Acta 52 (2007) 4825.
[14] Y. Ishikawa, T. Morita, K. Nakata, et al., J. Power Sources 163 (2007) 708.
[15] M. Sundaresan, R.M. Moore, J. Power Sources 145 (2005) 534.
[16] M. Khandelwal, S. Lee, M.M. Mench, J. Power Sources 172 (2007) 816.
[17] R.K. Ahluwalia, X. Wang, J. Power Sources 162 (2006) 502.
[18] L. Mao, C.Y. Wang, J. Electrochem. Soc. 154 (2007) B139.
[19] L. Mao, C.Y. Wang, J. Electrochem. Soc. 154 (2007) B341.
[20] H. Meng, J. Power Sources 162 (2006) 426.
[21] H. Meng, J. Power Sources 164 (2007) 688.
[22] H. Meng, J. Power Sources 168 (2007) 218.
[23] H. Meng, J. Power Sources 171 (2007) 738.
[24] H. Ju, H. Meng, C.Y. Wang, Int. J. Heat Mass Transfer 48 (2005) 1303.
[25] H. Wu, P. Berg, X. Li, J. Power Sources 165 (2007) 232.
[26] H. Meng, C.Y. Wang, J. Electrochem. Soc. 151 (2004) A358.
[27] H. Meng, J. Power Sources 161 (2006) 466.